Oral presentation | Data science and AI
Data science and AI-IV
Fri. Jul 19, 2024 10:45 AM - 12:45 PM Room C

[13-C-02] Turbulence Modeling with Field Inversion for a Slender Body at a Non-Zero Angle of Attack

*Yeji Yun[1], Seoyeon Heo[1], Junho Eom[1], Solkeun Jee[1] (1. Gwangju Institute of Science and Technology)

Keywords: Axisymmetric Slender Body, Field Inversion, Turbulence Modeling

Twelfth International Conference on
Computational Fluid Dynamics (ICCFD12),
Kobe, Japan, July 14-19, 2024

Turbulence Modeling with Field Inversion for a Slender Body at a Non-Zero Angle of Attack

Yeji Yun, Seoyeon Heo, Junho Eom, and Solkeun Jee†
†Corresponding author: sjee@gist.ac.kr
Gwangju Institute of Science and Technology (GIST), South Korea.

Abstract: The Spalart-Allmaras model is modified using field inversion for 3D separated flow around a slender body at a non-zero angle of attack. This study selects the flow around an axisymmetric body at a large enough angle of attack, where symmetric vortex pairs are generated in a crossflow direction. The SA model correction is optimized using experimental surface pressure as a target in the optimization cost function. The current study indicates that the model correction helps to represent the formation of major vortices and their separation from the slender body. The optimized SA correction decreases the turbulent viscosity before the flow separation, yielding early (and correct) separation location of the primary vortex. The model correction also represents the secondary vortex with the low pressure similarly measured in the experiment. The optimally-corrected SA simulation data are used for the machine learning process of the baseline SA model with local flow features. The trained model is tested with a new geometry and flow condition. The trained model improves the complex 3D separated flow around a new slender body. Further potential improvement in turbulence modeling is discussed in this study.

Keywords: aerodynamics, slender body, turbulence modeling, field inversion, vortex shedding

1 Introduction

Prediction capability of turbulent flow around a slender body is critical in designing a high-speed vehicle. It is particularly important to predict vortices formed around the body and flow separation. At a sufficiently high angle of attack, pairs of counter-rotating vortices form on the leeward side as shown in Fig. 1. The primary vortices often start to grow from the front (typically the nose of a slender body), whereas the secondary vortices appear around the cylinder aft body [1, 2, 3]. These vortices affect the pressure distribution on the body surface and eventually the aerodynamic forces and moments. In this study, a flow condition of symmetric vortex shedding phenomena at a non-zero angle of attack is considered for axisymmetric slender bodies.

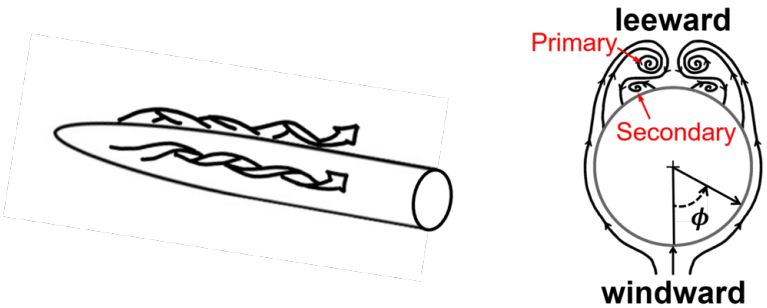

Figure 1: Schematic diagram of flow around an axisymmetric slender body (left) and major vortical structures at a cross section (right).

Reynolds-averaged Navier-Stokes (RANS) simulation has been used to study the aerodynamics of a slender body [2, 4, 5]. Murman and Chaderjian (1998) suggest a turbulence model correction to represent vortical structures formed around an axisymmetric body [2]. RANS studies of Degani et al. (1991) [4] and Birch et al. (2000) [5] indicate that further improvement is required in turbulence modeling because the computed aerodynamics forces depend on the choice of a turbulence RANS model. The well-known limitation of RANS simulation for generally separated flow [6] imposes a computational challenge for turbulent flow around a slender body at a high incidence. Typical RANS models are limited in predicting

the formation of major vortices and flow separation, resulting in unreliable estimation of surface pressure distribution and aerodynamic forces.

Recent studies have explored data-driven approaches to improve RANS turbulence models for separated flows [7, 8, 9, 10, 11, 12]. Nonetheless, recent attempts at turbulence model improvement lack of 3D separated flow, particularly flow around a slender body at a high enough angle of attack. Unlike 2D separated flow, such 3D flow involves vortex formation and detachment from a solid wall under the influence of crossflow. Previous studies primarily handle 2D flows such as flow around periodic hills [7, 8], airfoils [7] and axisymmetric base geometries [11].

This study aims to explore data-driven turbulence modeling for 3D separated flows, particularly 3D turbulent flow around an axisymmetric slender body at a non-zero angle of attack. Among various data-driven turbulence modeling methods, the field-inversion and machine learning (FIML) method [13] is used in this study. The FIML method allows to correct a turbulence model even with sparse data, not entire flow field data [14].

The rest of the paper is structured as follows. Section 2 describes the current computational setups, including grids, flow conditions, numerical schemes, and the FIML method for RANS model correction. Section 3.1 analyzes the model correction in comparison to the original model prediction, focusing on its impact on vortical shedding and changes in turbulent viscosity. In Section 3.2, the application of the model to a new geometry under different flow conditions using machine learning is discussed. Finally, Section 4 summarizes and concludes the findings of the study.

2 Methodology

Turbulent flow around axisymmetric slender bodies is simulated in RANS computations. Computational setups for the current simulation are described in Section 2.1. The turbulence model improvement with field inversion and machine learning (FIML) is described in Section 2.2.

2.1 Computational Setup for RANS Simulation

RANS computations are conducted for turbulent flow around slender bodies in this study. Since current flow conditions are associated with symmetric vortex shedding phenomena, steady RANS is pursued. The Spalart-Allmaras (SA) model is chosen for the baseline RANS model. The compressible RANS flow solver SU2 [15, 16] is used in this study. The James-Schmidt-Turkel scheme [17] is used for the convection fluxes of the compressible Navier-Stokes equations, and the corrected average-gradient scheme [15] is used for the viscous fluxes. Two slender bodies are simulated; one for the SA model training and the other for the test of the trained model.

2.1.1 Training case (Case 1)

The experiment of Lamont (1982) [18] is selected for Case 1 here. This case is used for training the SA model with field inversion data, i.e., the model correction. The flow conditions are as follows: the freestream Mach number is $M_\infty = 0.2$, the Reynolds number based on the body diameter D is $Re_D = 4 \times 10^6$, and the angle of attack $\alpha = 20°$. The length of the slender body is $L_b = 10.5D$ with the nose $L_n = 3.5D$ and the aft cylinder length $L_c = 7D$ as shown in Fig. 2a. Note that the cylinder extends by $3D$ downstream following the reference [2, 19] to exclude the wake from the simulation. The freestream is located sufficiently far from the body, following previous studies [2, 19]. The computational grid consists of 164 axial points, 72 radial points, and 120 circumferential points for the full-body configuration with the total grid count of about 1.4 million. Grid-convergence tests are conducted with two additional grids (data not included in this conference paper). The baseline SA model is used for Case 1 in the current field inversion process which allows to correct the model with target parameters. Then, the model correction is used to train (modify) the baseline SA model with a machine learning technique.

2.1.2 Test case (Case 2)

A new geometry with a new flow condition is selected in Case 2 to test the trained SA model. The ogive-cylinder body of Tinling and Allen (1962) [20] is chosen here (see Fig. 2b). Flow conditions are as follows: $M_\infty = 0.3$, $Re_D = 3 \times 10^6$, and $\alpha = 20°$. It should be noted that the test case is chosen for the similar flow condition of the training case. The body length is $L_b = 14D$ with the nose $L_n = 3.3D$ and the aft cylinder length $L_c = 10.7D$. Note that the cylinder body extends by $3.3D$ downstream to exclude

the wake in the simulation, following the similar approach of the reference [2, 19]. The computational grid for Case 2 consists of 137 axial points, 85 radial points, and 85 circumferential points, totaling about 1 million points. The prediction capability of the trained SA model is investigated with Case 2 using the same numerical scheme except for the turbulence model.

2.2 FIML method for RANS model correction

2.2.1 Field inversion

The field inversion method [13] is adopted to modify the baseline SA model in this study. Field inversion corrects a flow model by solving an optimization problem that minimizes a discrepancy between ground-truth data and the original model prediction for quantities of interest. An advantage of field inversion over other data-driven methods is its ability to correct a flow model even with sparse data without resorting to a dataset covering the whole flow field.

The current cost function consists of the discrepancy of the target parameter (here the pressure C_p) and the penalty term to mitigate an extreme correction. Here, pressure profiles at six axial positions from the experiment [18] are used in the cost function J as written in Eq. 1,

$$J(C_p) = \sum_{i=1}^{N}(C_{p,target} - C_{p,SA})^2 + \lambda \sum_{j=1}^{n}(\beta - 1)^2 \tag{1}$$

where N is the number of grid points of the selected axial pressure profiles, and n is the number of total grid points in the computational domain. The target pressure $C_{p,target}$ consists of experimental data primarily on the leeward side under adverse pressure gradients and RANS data near the stagnation line (i.e., $\phi = 0°$). The latter is required because the uncertainty in the experimental stagnation pressure [18] has been reported in the literature [2, 19, 4, 21]. The regularization factor is $\lambda = 10^{-10}$, small enough to minimize the discrepancy of the quantity of interest C_p in the optimization process without extreme correction β.

The SA model is modified using the model correction β multiplied to the production term of the model formula as written in Eq. 2.

$$\frac{D\hat{\nu}}{Dt} = \underbrace{\beta}_{Correction}\ \underbrace{c_{b1}\hat{S}\hat{\nu}}_{Production} - \underbrace{c_{w1}f_w(\frac{\hat{\nu}}{d})^2}_{Destruction} + \underbrace{\frac{1}{\sigma}[\nabla((\nu+\hat{\nu})\nabla\hat{\nu} + c_{b2}\nabla\hat{\nu})^2]}_{Diffusion} \tag{2}$$

where $\hat{\nu}$ is the SA model variable. The baseline SA model is the noft2 variant, and other notations in Eq. 2 are defined in the reference [22, 23]. The optimal model correction β is obtained as a result of the field inversion process and used as training data for the machine learning process.

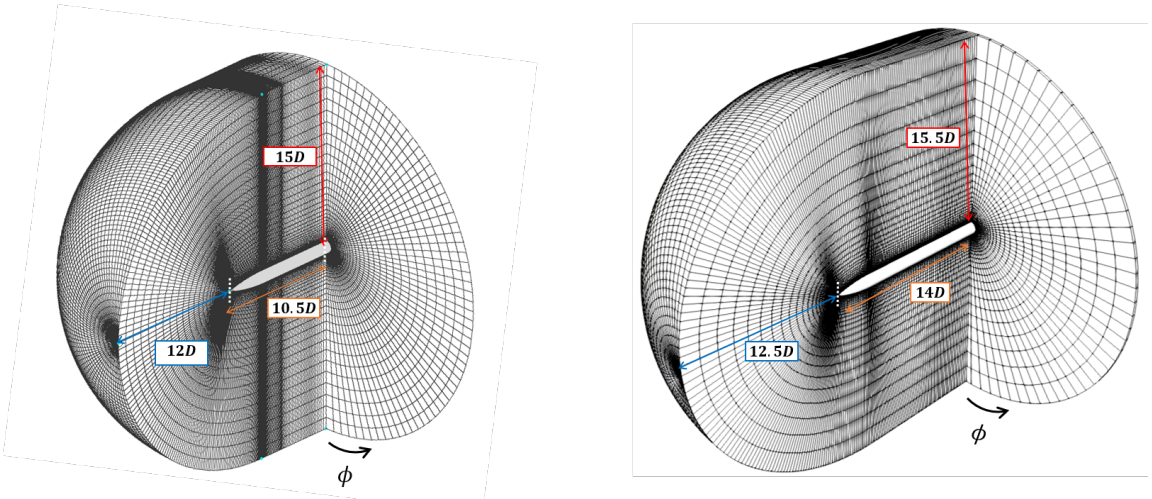

Figure 2: Computational grids of Case 1 (a) and 2 (b).

2.2.2 Machine learning

A fully connected neural network is employed to map the SA model correction β to local flow features η. The neural network consists of 6 hidden layers, each containing 100 nodes with tangent hyperbolic activation functions. The SA model correction β obtained from the field inversion process is used as the output of the neural network. The inputs for the network are local flow features η as listed in Table. 1. Here, Ω is the vorticity magnitude, S is the strain rate magnitude, d is the wall distance, U_i is the

Feature η	**Physical meaning**
$\frac{\Omega d}{\lvert U_i \rvert}$	Vorticity magnitude ($\Omega \equiv \sqrt{2\Omega_{ij}\Omega_{ij}}$)
$\frac{\Omega d^2}{\nu_t}$	Ratio of turbulent production and Destruction
$\frac{\Omega^2 - S^2}{S^2}$	Q criterion ($S \equiv \sqrt{2S_{ij}S_{ij}}$)
$\kappa \frac{\Omega}{d\sqrt{\frac{\partial \Omega}{\partial x_i}\frac{\partial \Omega}{\partial x_i}}}$	von Kármán length scale
$\frac{U_i U_j d}{\lvert U_k \rvert^3}\frac{\partial U_i}{\partial x_j}$	Deviation from parallel shear flow [24]
$\frac{U_i d}{0.5\rho \lvert U_j \rvert^3}\frac{\partial P}{\partial x_i}$	Pressure gradient in streamwise direction

Table 1: Flow feature η used in the current model training with machine learning

velocity, ν_t is the turbulent kinematic viscosity, ρ is the density, and P is the pressure. The set of current flow features is selected through the previous studies [10, 12].

3 Results and Discussion

The baseline SA model is corrected with the field inversion method using experimental pressure data in Section 3.1. The model correction β is a spatial function for the specific Case 1. Model training, i.e., mapping β into local flow features η, is conducted with the neural network in Section 3.2. The new geometry with the new flow condition (Case 2) is used to test the trained SA model for 3D turbulent separated flow around a slender body at a non-zero angle of attack.

3.1 SA Model Correction with Field Inversion

Pressure distribution at 7 selected axial locations is shown in Fig. 3. The original SA model struggles to represent the pressure distribution around the leeward side where adverse pressure gradients affect the flow separation and the formation of the vortices. The plateau around $\phi = 110°$ at $x/D = 4.5$ is associated with the flow separation, which is delayed in the RANS simulation with the original SA model. The second valley in the pressure distribution around $\phi = 160°$ is associated with the core of the secondary vortex. The low pressure measured in the experiment is not well captured with the original SA model in most of the axial stations.

In contrast to the original SA model, the optimized SA model reproduces the overall pressure profile. Note that the optimization of the model correction is pursued with experimentally measured pressure at 6 axial locations (excluding the pressure at $x/D = 5$). No significant modification is observed near the nose ($x/D = 0.5$) where there is no separation yet. The modification is visible in the pressure distribution after $x/D = 2$ as the primary vortex forms from the nose and separates, inducing the formation of the secondary vortex. The plateau of the pressure, indicating flow separation, is well incorporated in the optimized SA model. It is expected that the formation of the secondary vortex is better represented with the optimized SA model based on the good agreement of the second valley in the pressure distribution around $\phi = 160°$.

The current field inversion process yields a significant reduction of the pressure discrepancy included in the cost function $J(C_p)$ as shown in Fig. 4. The optimization process finds the model correction which reduces the initial discrepancy by about 60%. The pressure error (i.e., the first term in Eq. 1) at each axial location is shown in Fig. 4b. The majority of the pressure error is related to the four axial stations

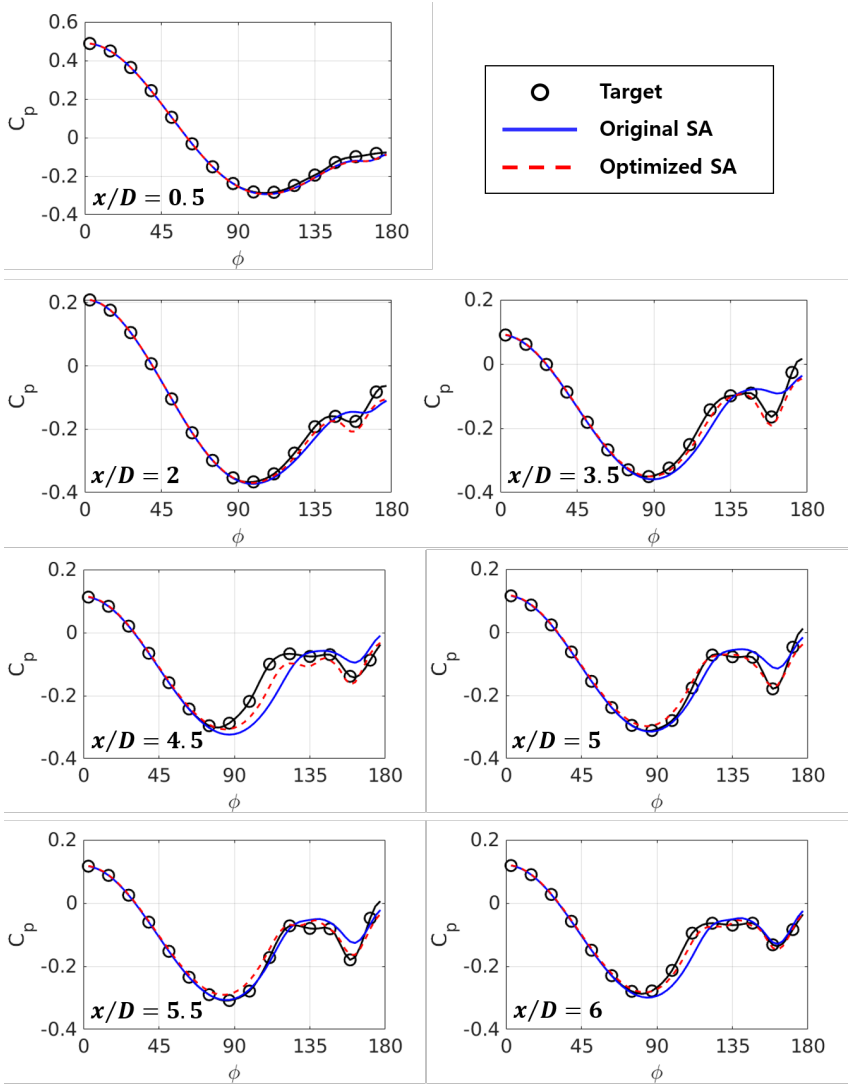

Figure 3: Pressure distributed along the roll angle ϕ at 7 selected axial locations for the target pressure based on the experiment [18], and the current computations of the original SA and the optimized SA models.

x/D =2, 3.5, 4.5, and 6. The pressure error at these stations drops significantly at the final iteration of the field inversion process.

Fig. 5 shows the SA correction β and the resulting vorticity field at three axial locations from the optimized SA model (field inversion). If $\beta \neq 1$, then the field inversion modifies the source term in the SA equation (Eq. 2). The blue and red regions in Fig. 5 imply the reduced and enhanced production of the model transport equation, respectively. The model correction β is lower than the unity in the leeward side at $x/D = 0.5$ as the primary vortex forms from the nose. The separation of the primary vortex is clearly visible at $x/D = 3.5$ as the secondary vortex forms near the wall under the primary vortex. The model correction β continuously reduces the turbulent production mostly on the leeward side before the primary vortex separates. At the downstream location $x/D = 6$, the production remains reduced with $\beta < 1$ before the flow separation. However, the model correction yields larger turbulent production with $\beta > 1$ for the separated flow sufficiently away from the body.

Adjusting turbulent production changes the turbulent viscosity μ_t in the flow field. The turbulent viscosity is compared between the original SA and the optimized SA models in Fig. 6. The significant reduction of μ_t is visible at $x/D = 3.5$ in Fig. 6 because the model correction is primarily $\beta < 1$ from the nose in Fig. 5. The turbulent viscosity of the optimized SA model remains smaller than the original SA counterpart in the downstream location $x/D = 6$ before the primary vortex sheds from the body. The current model correction yields larger μ_t in the separated flow sufficiently away from the wall.

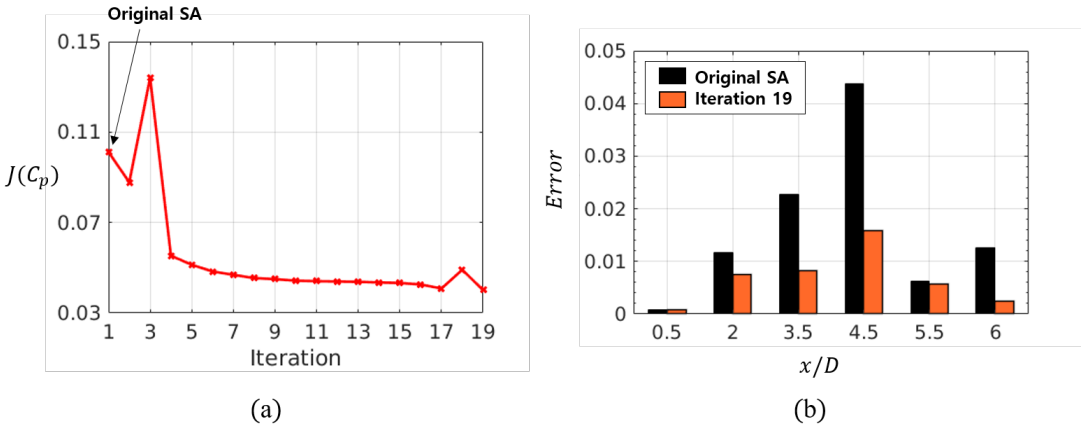

Figure 4: Decrease of the cost function $J(C_p)$ during the field inversion iteration (a) and the pressure error at each axial station at the final iteration (b).

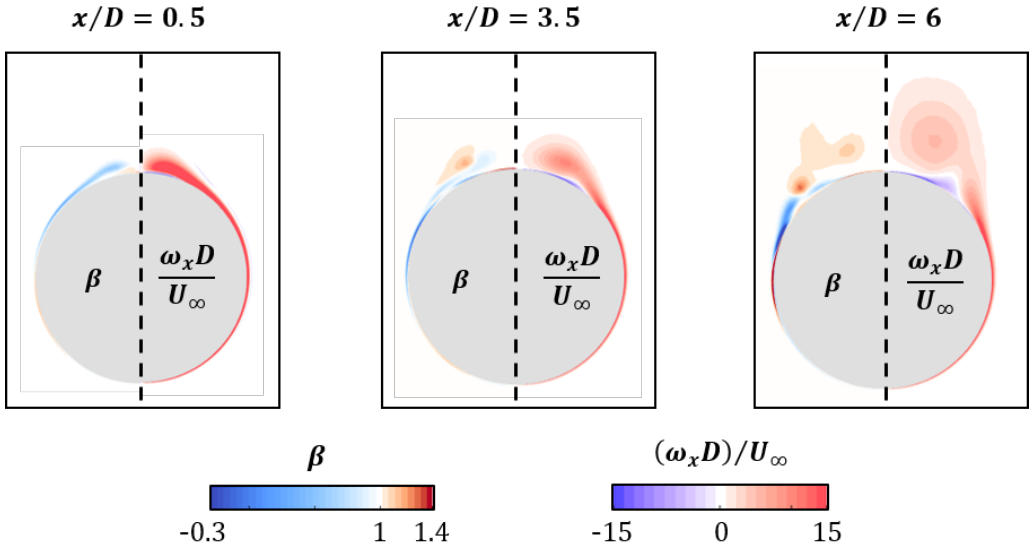

Figure 5: SA correction β and the dimensionless vorticity $\omega_x D/U_\infty$ from the optimized SA model in Case 1

Vortex formation and separation are further investigated with surface streamlines shown in Fig. 7. Note that the primary vortex starts to separate from the nose, whereas the secondary vortex mostly forms from the after cylinder body. The optimized SA model enhances the early formation of the primary vortex and its separation from the axisymmetric body. As a result, the primary separation line moves toward the windward direction. The secondary vortex also forms earlier in the optimized SA model, compared to the original SA model. Since no significant model correction around the bottom of the body where flow is well attached with a favorable pressure gradient, surface streamlines are similar between the original and optimized SA models.

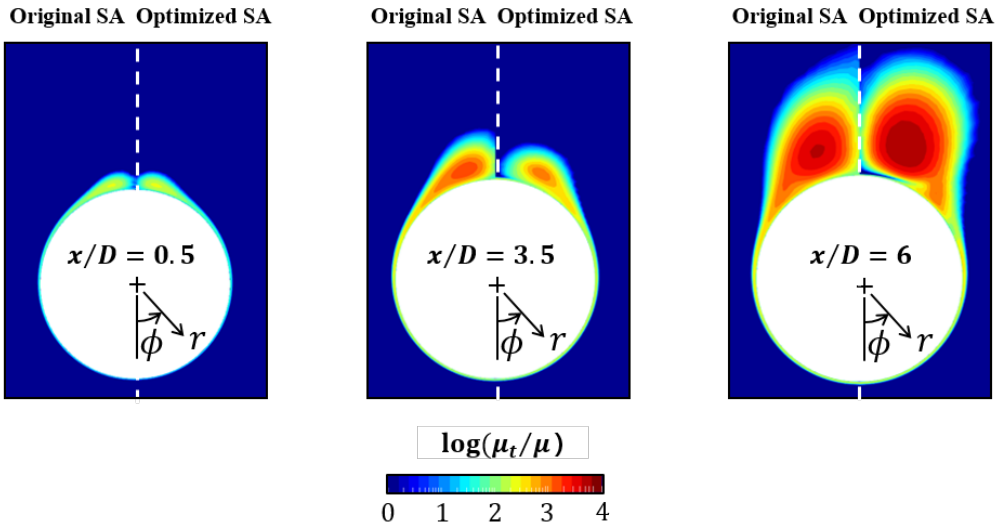

Figure 6: Turbulent viscosity μ_t (scaled by the molecular viscosity μ) from the original SA and the optimized SA models in Case 1

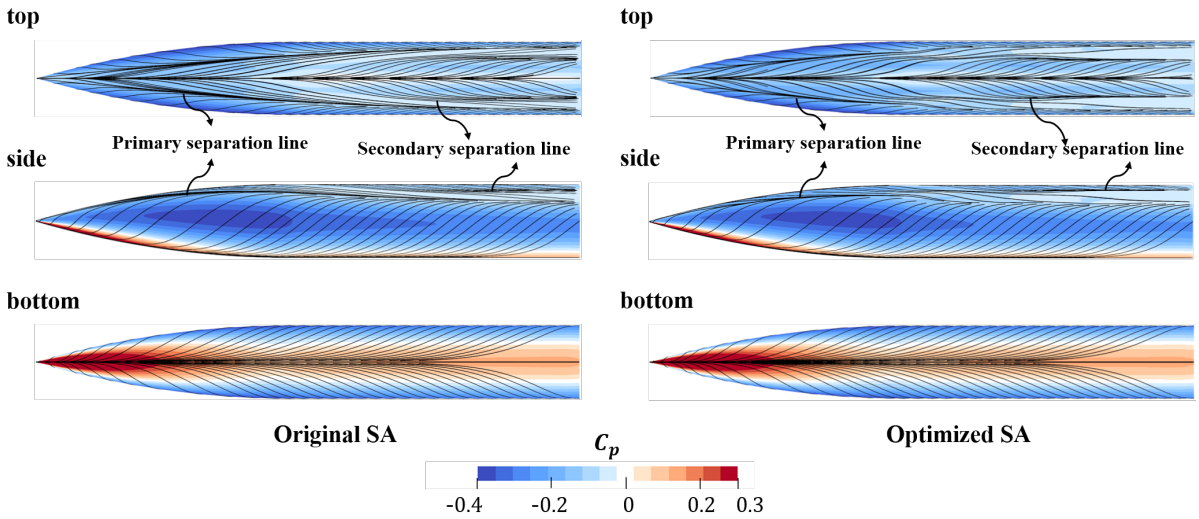

Figure 7: Surface streamlines with pressure contour of Case 1 from the original SA and the optimized SA models.

3.2 SA Model Correction with Machine Learning

RANS data with the optimized SA model in Case 1 are used to train the neural network, and the trained SA model is tested in Case 2 whose geometry and flow conditions are different from Case 1 (details documented in Section 2.1). The input of the neural network is the set of 6 local flow features described in Section 2.2.2, and the output is the SA model correction β. The machine learning process of the FIML method allows to map the model correction into the local flow features, providing a usable flow model for a new geometry such as Case 2 here.

The relevant experiment [20] provides surface profiles at 6 axial stations, so the prediction capability of the trained SA model is investigated with the available pressure data. Among them, three selected locations are used in Fig. 8 to demonstrate the improved prediction with the trained SA model. The pressure prediction is improved slightly on the nose $x/D = 2$ and significantly in the mid-cylinder body $x/D = 4.5$. The plateau of the pressure around $\phi = 120°$ at $x/D = 4.5$ is well captured with the trained SA model, indicating a better representation of the flow separation. The second pressure valley agrees well with the test data in the trained SA model, suggesting that the secondary vortex is well captured.

The turbulent viscosity μ_t is compared between the original and trained (modified) SA models in

Fig. 9 at the same three locations of Fig. 8. The trained SA model provides smaller μ_t before the primary vortex sheds from the body, which is consistent with the model correction observed in Case 1. The primary separation point at $x/D = 4.5$ (and separation line on the body surface) moves toward the windward direction with the trained SA model. For separated flow sufficiently far away from the body, μ_t increases, which is consistent with Case 1.

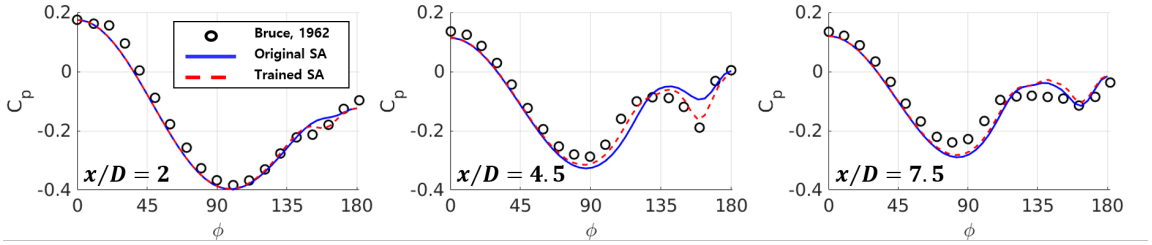

Figure 8: Pressure distributed along the roll angle ϕ at 3 selected axial locations from the experiment [20] and the current computations of the original SA and the optimized SA models.

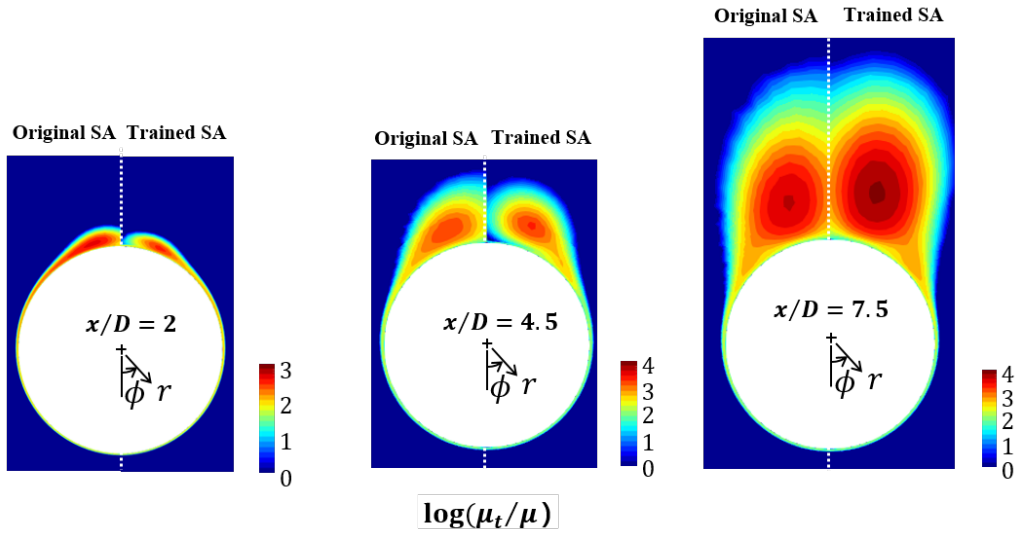

Figure 9: Turbulent viscosity μ_t (scaled by the molecular viscosity μ) from the original and trained SA models in Case 2

The separation of the primary vortex occurs earlier in the trained SA model compared to the original SA model (see the primary separation line in Fig. 10). The secondary vortex forms more upstream with the trained SA model, which is consistent with the earlier separation of the primary vortex.

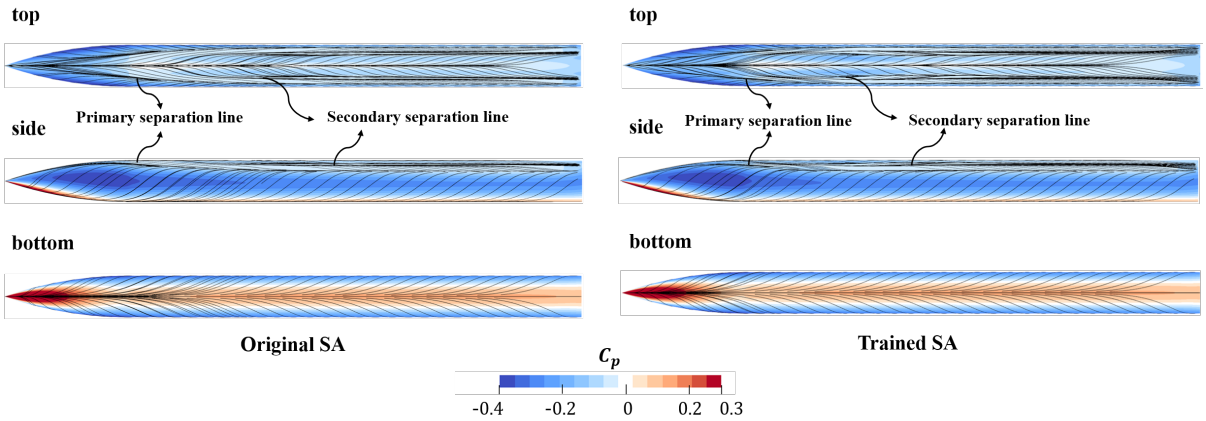

Figure 10: Surface streamlines with pressure contour of Case 2 from the original and trained SA models.

The trained SA model yields no significant change in the pressure prediction at the downstream station $x/D = 7.5$ (see Fig. 8). The modified turbulent viscosity shown in Fig. 9 is not sufficient enough to improve the pressure prediction associated with the flow separation around $\phi = 110^\circ$ and the pressure plateau. It is conjectured that important flow phenomena could be missed in the training case (Case 1) and exist in the test case (Case 2).

There are two types of vortical structures formed around a slender body at a non-zero angle of attack: vortices from the nose and the aft cylindrical body, which are indicated from surface streamlines in Figure 7 and 10. The geometry of Case 1 has a relatively short cylindrical body, therefore, the vortex developed from a nose tip primarily influences the flow field, especially on the surface pressure. In contrast, the geometry of Case 2 has a longer cylinder body than Case 1, therefore, not only the vortex from the nose but also the vortex separated from the body contributes to the downstream pressure simultaneously. It is suggested that if vortices detaching from the aft cylinder body are more incorporated in the model correction, then flow prediction could be improved for the downstream stations around a long slender body.

4 Conclusions

Axisymmetric slender bodies at a non-zero angle of attack are numerically simulated with a modified turbulence model in this study. The angle of attack is moderate to yield symmetric vortex shedding around a slender body. The Spalart-Allmaras model is modified to capture the vortex shedding phenomena using the field inversion method. Pressure distributions on the surface of a slender body are chosen for the optimization cost function used in field inversion. The field inversion process adjusts the balance of the SA source terms, resulting in a good agreement to experimental pressure data associated with the formation of vortices and flow separation.

The neural-network-based machine learning method is used to train the corrected turbulence model with generic flow features. The trained turbulence model with one axisymmetric body (Case 1) is tested for the second body (Case 2) with different flow conditions. The trained model improves the prediction capability of the formation of the primary and secondary vortices. The current study indicates that the current modeling approach with field inversion and machine learning is promising in improving a turbulence model for complex 3D separated flow.

Acknowledgment

This work was supported by Data-Driven Flow Modeling Research Laboratory funded by Defense Acquisition Program Administration under Grant UD230015SD.

References

[1] E. R. Keener. Oil flow separation patterns on an ogive forebody. *AIAA Journal*, 21(4):550–556, 1983.

[2] S. Murman and N. Chaderjian. Application of turbulence models to separated high-angle-of-attack flows. In *AIAA 23rd Atmospheric Flight Mechanics Conference*, page 4519, 1998.

[3] R. M. Cummings, J. R. Forsythe, S. A. Morton, and K. D. Squires. Computational challenges in high angle of attack flow prediction. *Progress in Aerospace Sciences*, 39(5):369–384, 2003.

[4] D. Degani, L. B. Schiff, and Y. Levy. Numerical prediction of subsonic turbulent flows over slender bodiesat high incidence. *AIAA Journal*, 29(12):2054–2061, 1991.

[5] T. Birch, I. Wrisdale, and S. Prince. CFD predictions of missile flowfields. In *AIAA 18th Applied Aerodynamics Conference*, page 4211, 2000.

[6] J. R. Chawner. Progress toward realizing the CFD vision 2030. In *11th International Conference on Computational Fluid Dynamics ICCFD11*, 2022.

[7] A. P. Singh, S. Medida, and K. Duraisamy. Machine-learning-augmented predictive modeling of turbulent separated flows over airfoils. *AIAA Journal*, 55(7):2215–2227, 2017.

[8] C. Yan, H. Li, Y. Zhang, and H. Chen. Data-driven turbulence modeling in separated flows considering physical mechanism analysis. *International Journal of Heat and Fluid Flow*, 96:109004, 2022.

[9] C. L. Rumsey, G. N. Coleman, and L. Wang. In search of data-driven improvements to RANS models applied to separated flows. In *AIAA SciTech 2022 Forum*, 2022.

[10] S. Heo, Y. Yun, M. Jeong, J. Park, D. Kim, S. Jee, S. Lee, and J. S. Park. Improvement of a turbulence model for subsonic and supersonic flows around axisymmetric bodies. In *The Korean Society for Aeronautical and Space Sciences (KSAS) 2023 Fall Conference*, 2023.

[11] S. Heo, Y. Yun, M. Jeong, and S. Jee. Simulation of supersonic axisymmetric base flow with a data-driven turbulence model. *Aerospace Science and Technology*, 147:109014, 2024.

[12] S. Heo, Y. Yun, and S. Jee. Data-driven turbulence modeling for separated flow around axisymmetric bodies. In *ERCOFTAC Workshop on Machine Learning for Fluid Dynamics*, 2024.

[13] E. J. Parish and K. Duraisamy. A paradigm for data-driven predictive modeling using field inversion and machine learning. *Journal of Computational Physics*, 305:758–774, 2016.

[14] K. Duraisamy, G. Iaccarino, and H. Xiao. Turbulence modeling in the age of data. *Annual Review of Fluid Mechanics*, 51(1):357–377, 2019.

[15] F. Palacios, T. D. Economon, A. Aranake, S. R. Copeland, A. K. Lonkar, T. W. Lukaczyk, D. E. Manosalvas, K. R. Naik, S. Padron, B. Tracey, A. Variyar, and J. J. Alonso. Stanford university unstructured (SU2): Analysis and design technology for turbulent flows. In *AIAA SciTech 52nd Aerospace Sciences Meeting*, 2014.

[16] T. D. Economon, F. Palacios, S. R. Copeland, T. W. Lukaczyk, and J. J. Alonso. Su2: An open-source suite for multiphysics simulation and design. *AIAA Journal*, 54(3):828–846, 2016.

[17] A. Jameson, W. Schmidt, and E. Turkel. Numerical solution of the euler equations by finite volume methods using runge kutta time stepping schemes. In *AIAA 14th Fluid and Plasma Dynamics Conference*, 1981.

[18] P. Lamont. The complex asymmetric flow over a 3.5D ogive nose and cylindrical afterbody at high angles of attack. In *AIAA 20th Aerospace Sciences Meeting*, 1982.

[19] S. Murman. Vortex filtering for turbulence models applied to crossflow separation. In *AIAA 39th Aerospace Sciences Meeting and Exhibit*, page 114, 2001.

[20] B. E. Tinling and C. Q. Allen. An investigation of the normal-force and vortex-wake characteristics of an ogive-cylinder body at subsonic speeds. Technical Report NASA TN D-1297, National Aeronautics and Space Administration, 1962.

[21] P. M. Hartwich and R. M. Hall. Navier-stokes solutions for vortical flows over a tangent-ogive cylinder. *AIAA Journal*, 28(7):1171–1179, 1990.

[22] B. Aupoix and P. R. Spalart. Extensions of the Spalart–Allmaras turbulence model to account for wall roughness. *International Journal of Heat and Fluid Flow*, 24(4):454–462, 2003. Selected Papers from the Fifth International Conference on Engineering Turbulence Modelling and Measurements.

[23] P. Spalart and S. Allmaras. A one-equation turbulence model for aerodynamic flows. In *AIAA 30th Aerospace Sciences Meeting and Exhibit*, page 432, 1992.

[24] C. Gorlé, J. Larsson, M. Emory, and G. Iaccarino. The deviation from parallel shear flow as an indicator of linear eddy-viscosity model inaccuracy. *Physics of Fluids*, 26(5):051702, 05 2014.